Chapter 5

Application and Challenges of Signal Processing Techniques for Lamb Waves Structural Integrity Evaluation: Part B-Defects Imaging and Recognition Techniques

Zenghua Liu and Honglei Chen

Additional information is available at the end of the chapter

http://dx.doi.org/10.5772/intechopen.79475

Abstract

The wavefield of Lamb waves is yielded by the feature of plate-like structures. And many defects imaging techniques and intelligent recognition algorithms have been developed for defects location, sizing and recognition through analyzing the parameters of received Lamb waves signals including the arrival time, attenuation, amplitude and phase, etc. In this chapter, we give a briefly review about the defects imaging techniques and the intelligent recognition algorithms. Considering the available parameters of Lamb waves signals and the setting of detection/monitoring systems, we roughly divide the defect location and sizing techniques into four categories, including the sparse array imaging techniques, the tomography techniques, the compact array techniques, and full wavefield imaging techniques. The principle of them is introduced. Meanwhile, the intelligent recognition techniques based on various of intelligent recognition algorithms that have been widely used to analyze Lamb waves signals in the research of defect recognition are reviewed, including the support vector machine, Bayesian methodology, and the neural networks.

Keywords: Lamb waves, plate, defect imaging techniques, intelligent detection algorithm, structural integrity evaluation

1. Introduction

The propagation characteristic of Lamb waves is yielded by the state of plate-like structures. Defect scattering waveforms are generated as the interaction between Lamb waves and

defects, and that may be contained in received Lamb waves signals during the Lamb waves structural integrity evaluation. To clearly show out the state of the structures, many kinds of defect imaging and recognition techniques are proposed for analyzing the change of the signal parameters based on the settings of detection/monitoring systems during the past decades. In laboratory and practical field applications of Lamb waves based structure integrity evaluation, the detection/monitoring systems have two basic setting strategies. Firstly, Lamb waves signals are emitted and sensed at relatively small number of spatially distributed position by transducers that have the same or different transduction mechanisms. These positions are maybe distributed in sparse (adjacent transducer spacing is larger than the largest wavelength of signals) or compact (adjacent transducer spacing is shorter than the shortest wavelength of signals) array forms. Collaborative with different signal excitation and detection strategies, signal processing techniques are developed for integrity detection/monitoring in the whole structure. The other strategy is a full-scale scanning of the surface of structures with laser ultrasonic systems, air-coupled scanning systems, to obtain the full wavefield of Lamb waves. On the basis of the above detection/monitoring system setting strategies, Lamb waves signals used for damage detection/monitoring are obtained. Then, signal processing techniques are adopted to analyze the change of signal parameters to extract the damage information such as the amplitudes, velocity, phase, frequency, etc. Finally, defect influence maps and intelligent recognition models that indicating defect information are achieved with imaging and recognition techniques.

In this chapter, the defect imaging techniques and intelligent recognition techniques are briefly reviewed. Considering the settings of detection/monitoring system, we roughly divide the defect imaging algorithms into four categories: spare array imaging techniques, tomography techniques, compact array imaging techniques, and full wavefield imaging techniques. The basic principle of them is introduced in Section 2. In Section 3, the intelligent recognition techniques used to process Lamb waves signals and defect feature recognition are introduced. Finally, a short summary and conclusion are provided.

2. Defect imaging techniques

When a set of Lamb waves signals are received at spatially distributed positions, the techniques map the received time-domain signals that have or have not been processed with the signal optimization techniques into a 2D or 3D space-domain based on the ToF or beam directivity for defect location (sizing are termed the defect imaging techniques). Considering the distribution of the signal received position, we roughly divide these techniques into four categories: sparse array imaging techniques, tomography techniques, compact array imaging techniques, and full wavefield imaging techniques.

2.1. Sparse array imaging techniques

In a sparse array, the adjacent transducers are far separated from each other that provide higher coverage with fewer transducers at the cost of imaging resolution. Discrete ellipse

http://dx.doi.org/10.5772/intechopen.79475

imaging technique [1, 2] and the hyperbola imaging technique [3] are ToF imaging algorithms and map the amplitude information of scattering signals to elliptical trajectory and hyperbola trajectory, respectively. Their calculation formulas are expressed as

$$t_{ij} = \begin{cases} \left(\sqrt{(x_i - x)^2 + (y_i - y)^2} + \sqrt{(x_j - x)^2 + \left(y_j - y\right)^2}\right)/c_g, & \text{(Elliptical trajectory)} \\ \left(\sqrt{(x_i - x)^2 + (y_i - y)^2} - \sqrt{(x_j - x)^2 + \left(y_j - y\right)^2}\right)/c_g, & \text{(Hyperbola trajecory)} \end{cases}, \quad (1)$$

In the process, the previously recorded baseline data are subtracted from the field-sensing signals. Then, the pixel intensity is determined by calculating the amplitude information contained in the combined backward signals. Both of the algorithms have full summation form and full multiplication form and can be expressed as

$$I(x,y) = \begin{cases} \frac{1}{N^2}\sum_{i=1}^{N}\sum_{j=1,\, i\neq j}^{N} s_{ij}\left(t_{ij}[x,y]\right), & \text{(Full summation)} \\ \frac{1}{N^2}\prod_{i=1}^{N}\prod_{j=1,\, i\neq j}^{N} s_{ij}\left(t_{ij}[x,y]\right), & \text{(Full multiplicaton)} \end{cases}, \quad (2)$$

where N is the number of transducers, s_{ij} is the amplitude information of scattering signals, t_{ij} is the arrival time of scattering signals. The quality of image produced improves rapidly with the increase of the transducer number.

The window-modulated ellipse imaging algorithm is proposed in Ref. [4]. Many auxiliary signal processing techniques are developed for enhancing the imaging performance, such as the scattering signal normalization to eliminate the different path sensitivity to damage and extract damage information with the complex Morlet wavelet coefficient [5], the temperature effect compensation technique to ensure the detection quality [6], consideration of the velocity directionality [2], and damage information extraction with statistical method [7, 8].

2.2. Tomography techniques

Tomography technique works with specific designed transducer array to reconstruct a physical quantity in a cross-sectional area by analyzing Lamb waves attenuation, velocity, and mode conversion from the projection of the quantity in all directions. There are three classical transducer configuration existed in tomographic detection, parallel tomography, fan beam tomography, and crosshole tomography [9]. **Figure 1** plots the typical spatial distributions of transducers working with different tomography mechanisms in which the parallel array working with a parallel tomography at 0°, circular array working with fan beam tomography at 0°, and square array working with crosshole tomography are shown in **Figure 1(a)**, **(b)** and **(c)**, respectively. In the parallel array, the transducers are scanned along parallel lines. Once the pitch-catch measurements for each ray in an individual orientation have been taken, the sample is rotated by a fixed amount and the measurement is repeated. The ray density is

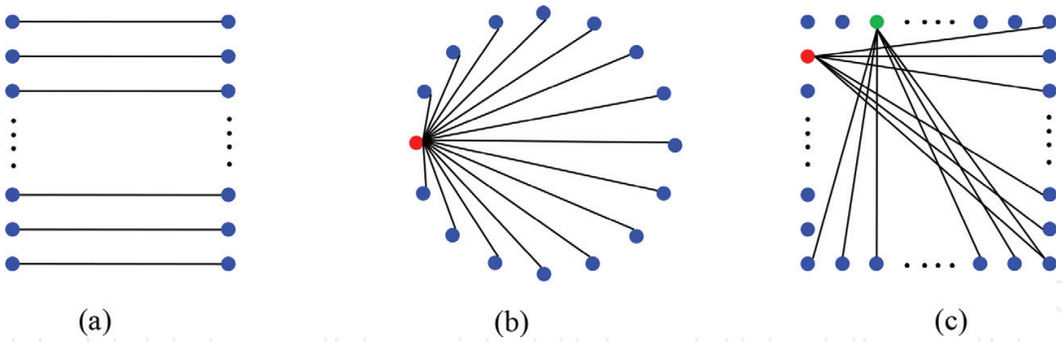

Figure 1. Typical spatial distributions of transducers working with different tomography mechanisms. (a) Parallel array working with a parallel tomography at 0°, (b) circular array working with fan beam tomography at 0°, and (c) square array working with crosshole tomography.

uniform for parallel projection tomography within the scanning region that is critical to the quality of the reconstruction. Crosshole configuration is a fast and practical alternative to the parallel-projection scheme in which transducers surround the detection zone to improve the ray density. The classical tomographic image reconstruction algorithms have the probabilistic reconstruction algorithms, transform methods, and iteration-based algorithms.

The probabilistic reconstruction algorithms (PRAs) are processed with the probabilistic statistical techniques to analyze the difference among the parameters for all the rays, including the ToF, waveforms, and energy [10]. The PRA has the flexibility in array geometry selection that can realize good reconstruction quality in fast speed. In the analysis, the ray theory needs to satisfy two validity criteria: the geometry size of the defect must be larger than the wavelength and larger than the width of the Fresnel zone. The waveform overlapping caused by reflection echoes of multidefects may make the TOF calculation inaccurate and fail the ray theory. The probabilistic inspection of damage (RAPID) [11, 12] method is a typical PRA that has been studied in Lamb waves based structure integrity evaluation in which variable shape factor is used for irregular shape defect imaging [13]. Keulen et al. [14] introduced the damage progression history into RAPID for composite structure detection. Sheen et al. [15] modified the shape factor, β, of RAPID algorithm to quantify a defect area. The expressions of the RAPID algorithm are

$$I_{\mathrm{RAPID}}(x,y) = \sum_{n=1}^{N} \left(1 - \rho_n^{ij}(x,y)\right) W_n\left[R_n^{ij}(x,y)\right], \tag{3}$$

$$W_n\left[R_n^{ij}(x,y)\right] = \begin{cases} 1 - \dfrac{R_n^{ij}(x,y)}{\beta}, & R_n^{ij}(x,y) \le \beta \\ 0 \quad , & R_n^{ij}(x,y) > \beta \end{cases}, \tag{4}$$

$$R_n^{ij}(x,y) = \frac{\sqrt{(x_i - x)^2 + (y_i - y)^2} + \sqrt{(x_j - x)^2 + (y_j - y)^2}}{\sqrt{(x_i - x_j)^2 + (y_i - y_j)^2}} - 1, \tag{5}$$

where $I_{\mathrm{RAPID}}(x,y)$ is the pixel value in the imaging zone, ρ is the zero-lag cross correlation between the baseline data and the received signals, W_n is the weighted distribution function, n

http://dx.doi.org/10.5772/intechopen.79475

is the path number of the pitch-catch transducers numbered as i and j, respectively, $R_n^{ij}(x,y)$ is related to both the distance from point (x, y) to the two transducers for excitation (x_i, y_i) and sensing (x_j, y_j) and the distance between the two transducers, β controls the size of the ellipse and $\beta > 1$. If β is too small, then artifacts will be introduced. If it is too large, the resolution will be lost. Usually, β is setting around 1.05 [16]. The technique for relative relationship calculation algorithms can be used to acquire the value of ρ, such as correlation coefficient method, time reversal method, baseline subtraction method, etc. More damage index calculation methods are reviewed in [17].

Filtered back-projection (FBP) combines the back-projection and the filter based on the Radon transform and Fourier slice theorem. Only with a circular sensor array, FBP method has efficiency of reconstruction and incomplete datasets, and unfortunately is sensitive to noise. It is essential to form a complete set of projections from many directions. Its formulas can be expressed as

$$I_{\mathrm{FBP}}(x,y) = \int_0^{2\pi} \int_{-\infty}^{+\infty} F(\omega,\theta) e^{i2\pi\omega(x\cos\theta + y\sin\theta)} \omega d\omega d\theta = \int_0^{\pi} Q_\theta(t) d\theta, \tag{6}$$

$$Q_\theta(t) = \int_{-\infty}^{+\infty} F(\omega,\theta) e^{i2\pi\omega t} |\omega| d\omega, \tag{7}$$

where $I_{\mathrm{FBP}}(x,y)$ is the pixel value in the imaging zone, $F(\omega,\theta)$ is the spatial Fourier transform of a line integral of the attenuation $f(x,y)$ in a polar coordinate system o-θ, $Q_\theta(t)$ is called a filtered projection because it represents a spatial frequency filtering operation, in which the filter response is $|\omega|$. Every point (x,y) in the image plane is contributed by a value $Q_\theta(t)$ from all direction θ. For a given direction θ, the function $Q_\theta(t)$ is a constant on the line AB, where t is fixed as shown in **Figure 2(a)**. This is equivalent to saying that the filtered projection function $Q_\theta(t)$, which is obtained from angle θ and position t, is back-projected along the initial projection direction over the image plane.

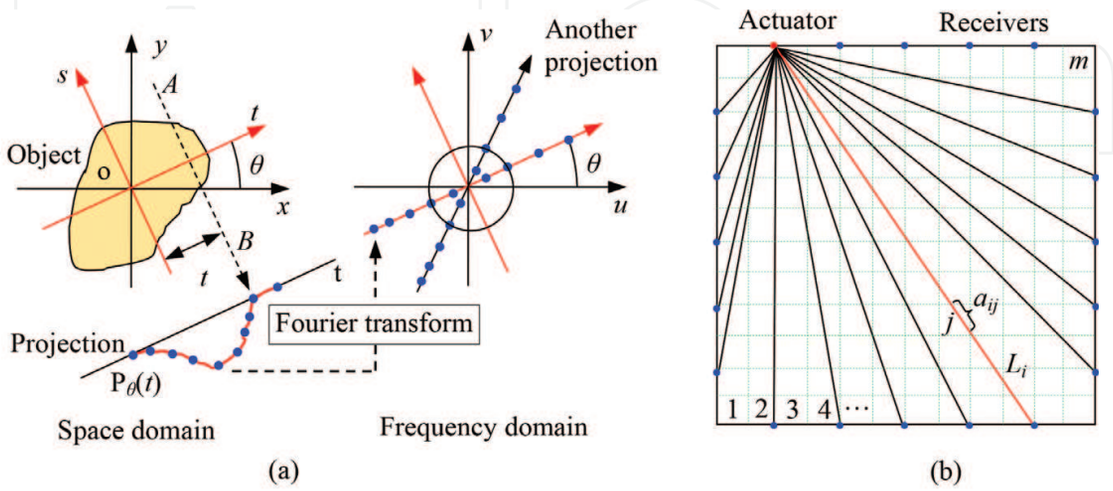

Figure 2. Principle of fan beam projection and algebraic reconstruction technique. (a) Principle of the filtered back-projection method and (b) situation of the ith path crossing the specimen.

The key to FBP tomographic image is the Fourier slice theorem that relates the measured projection data to the 2D Fourier transform of the object cross section. Wright et al. [18] used the FBP technique to image defects in isotropic and anisotropic plates of different materials using air-coupled Lamb wave tomography. Mokhtari et al. [19] proposed a polygon reconstruction technique for polygonal damage shape reconstruction. First, the projections (Radon transform) of the damaged region are generated from a small number of angles with the aid of beamforming method. Then, the damaged region is modeled by a polygon, which its optimal number of vertices is estimated using the minimum description length principle. Finally, using the polygon reconstruction technique, the coordinates of the vertices are determined. While in practice, it is not possible to measure a large number of projections in FBP that may induce the aliasing distortions by insufficiency of the input data, necessary for the transform-based techniques to produce highly accurate results. Researchers developed the interpolated FBP in which interpolations with respect to sample angle and projection angle based on limit measurements are used to generate the required projection data for the number of sampled grid values necessary for displaying a well-balanced reconstructed image. Meanwhile, it should constrain the projection data at a source point to zero when using the interpolation, rather than using extrapolation to generate projection data. **Figure 2(a)** plots the principle of the filtered back-projection method [20]. The formula, $I_{\text{fan\_FBP}}(x, y)$, of the fan beam-based FBP can be expressed as

$$I_{\text{fan\_FBP}}(x, y) = \frac{2\pi}{M} \sum_{i=1}^{M} \frac{Q_{\beta i}(\gamma)}{L^2(x, y, \beta_i)}, \tag{8}$$

where $Q_{\beta i}(n\alpha)$ is the filtered projection along the fan, M is the number of projections, and L is the distance from the transmitter to the point (x,y). β_i is the i^{th} projection angle and γ is the angle of the fan beam ray passing through the point (x,y).

The algebraic reconstruction technique (ART) starts from an initial guess for the reconstructed object and then performs a sequence of iterative grid projections and correction back-projections until the reconstruction has converged. Its formulae are expressed in Eqs. (9)–(11).

$$A_{i\times j} \times x_{j\times 1} = b_{i\times 1} \tag{9}$$

$$b_{i\times 1} = \int_j X(i,j) dl_{ij} \tag{10}$$

$$\begin{pmatrix} b_1 \\ \vdots \\ b_i \\ \vdots \\ b_m \end{pmatrix} = k \begin{pmatrix} L_{11} & \cdots & L_{1j} & \cdots & L_{1n} \\ \vdots & & \vdots & & \vdots \\ L_{i1} & \cdots & L_{ij} & & L_{mj} \\ \vdots & & \vdots & & \vdots \\ L_{m1} & \cdots & L_{mj} & \cdots & L_{mn} \end{pmatrix} \begin{pmatrix} x_1 \\ \vdots \\ x_i \\ \vdots \\ x_m \end{pmatrix} \tag{11}$$

where $A_{i\times j}$ represents the weight of i^{th} path in j^{th} grid, x represents the image results for each cell, and $b_{i\ \times\ 1}$ represents the change of signal feature (correlation) for each path. $X(i,j)$ is the

http://dx.doi.org/10.5772/intechopen.79475

attenuation coefficient for i^{th} path in j^{th} grid, and the L_{ij} represents the real length for i^{th} projected to j^{th} grid. Here, m represents the number of paths and n represents the number of grids.

In the ART, a weight matrix is constructed as a rectangular array whose size is equal to the number of paths multiplied by the number of grids. From the projections (measured data) and the weight matrix (created from sensor locations and ray geometry), the field value that maps the state of the inspection zone (correlation coefficient) is obtained using the ART method. The iterative solution to the reconstruction problem in ART is constructed by Ladas and Deveaney [21]. The iteration operation of Eq. (9) is expressed as Eq. (12) [23] in which one equation is used in each step, and an iteration consists of m steps.

$$\begin{aligned} x^{k,0} &= x^k \\ x^{k,i} &= x^{k,i-1} + \lambda_k \frac{b_i - a^i x^{k,i-1}}{\|a^i\|_2^2}, \ i = 1, 2, \cdots, m \\ x^{k+1} &= x^{k,m} \end{aligned} \tag{12}$$

Though compared with the FBP technique, ART has many advantages including better noise tolerance and better handling of the insufficiently distributed projection datasets that are induced by the spare and nonuniformly distributed projection data, it has slow speed due to iteration process. Wang et al. [22] used the ART to locate and quantify the corrosion damage at the edge of holes. In order to make the tomographic image describe the real condition of the damage, a homogenization method was designed to make the image smoother. Improved tomograms as a result of ART consider the anisotropic and attenuation characteristics of composite plates [23]. The technique based on the similarity theory is the simultaneous iterative reconstruction technique (SIRT). Malyarenko et al. [24] described the basic principle of SIRT for Lamb waves tomography that working with travel time data. In the research, the bend ray routines of a moderately scattered wavefiled was transformed into straight routines with a ray bending correction technique. The output image from the present straight ray algorithm serves as an input background for the ray tracing routine. The curved-ray ART then reconstructs the updated image and feed the next iteration until the desired quality or asymptotic behavior is observed. Miller et al. [25] used SIRT to process the multiple-mode Lamb wave signals for feature extraction of corrosion thinning for autonomous classification of flaw severity. This technique also termed diffraction tomography (DT) technique incorporates scattering effect into tomographic algorithms in order to improve the image quality and resolution. Mode conversion frequency occurs on defect boundaries, and dispersion makes all quantities frequency dependent.

Figure 3 plots the stages of accuracy thickness mapping tomography algorithms. Inhomogeneity objects are as small as 5% of the background; multiple scattering can introduce severe distortions in multicomponent objects [26]. The hybrid algorithm for robust breast ultrasound tomography (HARBUT) uses the low-resolution bent-ray tomography algorithm as the background for DT [27] in which bent-ray tomography can be applied initially to obtain a low-resolution estimate of the velocity field; this then forms the background for the DT method using the technique outlined above. Meanwhile, the subtraction is not necessary to obtain a

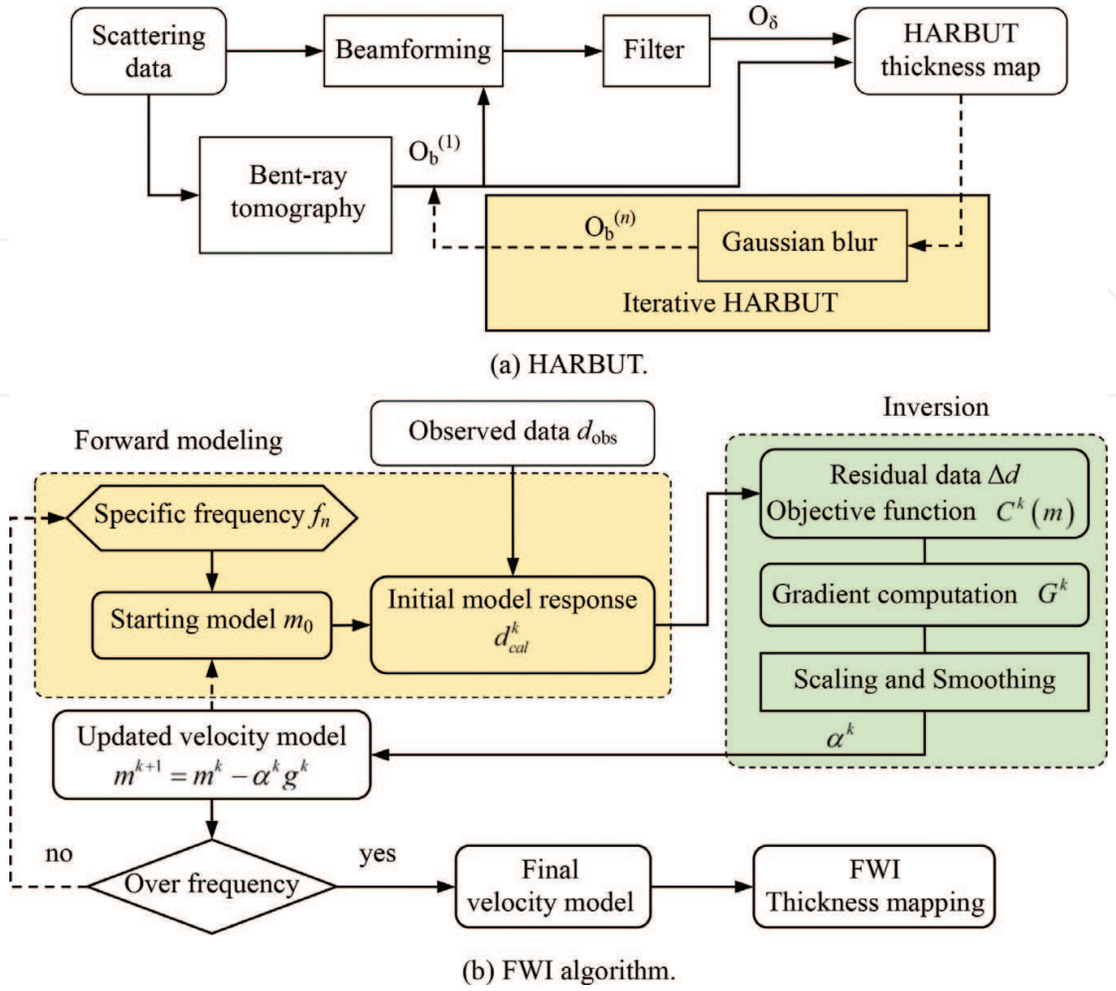

Figure 3. Stages of accuracy thickness mapping tomography algorithms. (a) HARBUT. (b) FWI algorithm.

good reconstruction, simplifying the process and avoiding these errors. The object function in HARBUT is divided into two components, the known background component O_b and the perturbation component O_δ. Since there is no need to run forward models, the speed of the algorithm is also improved. While the traditional HARBUT relies on having a sufficiently accurate background reconstruction that should satisfy the Born approximation assumption, iterating HARBUT uses an existing HARBUT reconstruction as the background for another HARBUT stage in place of bent-ray tomography, as illustrated in **Figure 3(a)**. At each step, O_b becomes more accurate, minimizing O_δ and allowing HARBUT to produce more accurate velocity maps. Through iteration operation of the HARBUT, small and high contrast defects are successfully imaged. A Gaussian filter is used to smooth the background before the next iteration, which is a form of regularization. This filter aims to remove as many of the artifacts from each iteration as possible, while maintaining the true reconstruction values. Full waveform inversion (FWI) technique is first developed in geophysics for seismic wave imaging in which the process also based on a serious of iteration operation. Rao et al. [28] introduced the FWI in Lamb waves tomography for corrosion mapping. The stages for FWI algorithm is plotted in **Figure 3(b)** in which a numerical forward model is used to predict the scattering of

http://dx.doi.org/10.5772/intechopen.79475

Lamb waves through corrosion defects and an iterative inverse model to reconstruct the corrosion profile. The aim of the tomography is to reconstruct the object function, which is a mathematical representation of the defect and is formulated in terms of velocity. The FWI algorithm proceeds from a starting velocity model to refine the velocity model in order to reduce the residual wavefield between the predicted data by the current model and the observed data from FE simulations or experiments. The predicted data are obtained by using frequency-domain finite difference method. It overcomes the limitation imposed by ignoring crucial low-frequency effects in travel time tomography. The FWI can obtain a resolution of around 0.7 wavelengths for defects with smooth depth variations from the acoustic modeling data, and about 1.5∼2.0 wavelengths from the elastic modeling data. The defect abrupt change in the wall thickness has been shown to decrease the reconstruction error of small defects compared to the smoothly varying thickness, for larger defects with sharper change in thickness, they are more likely to lead to overestimation in depth [29]. FWI allows higher order diffraction and scattering to be considered in its numerical solver, thus it has the potential to achieve more accurate inversion results, especially when multiple defects exist.

2.3. Compact array imaging techniques

Phase array (PA) technique and the synthetic aperture (SA) technique are widely performed based on the compact arrays in which the spacing between the adjacent transducers is shorter than the wavelength. **Figure 4** plots the typical compact arrays used for Lamb waves based structure integrity evaluation, such as the linear-phased arrays, circular, square, spiral, and star-shaped arrays [30]. During detection or monitoring, when one of the transducers used as actuator, Lamb waves signals are captured by all the rest transducers, then next transducer is chosen and used as actuator and capture the signal data until all the transducers have been

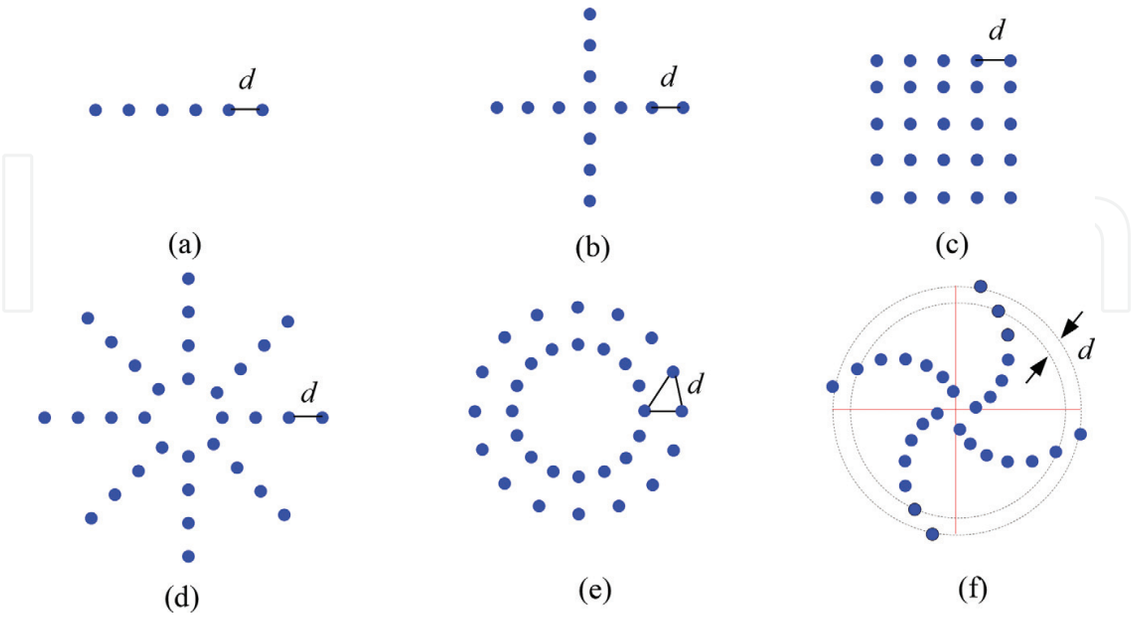

Figure 4. Typical compact arrays used for Lamb waves based structure integrity evaluation. (a) Linear, (b) cross-shaped, (c) rectangular, (d) star-shaped, (e) circular, and (f) spiral.

used for Lamb waves emitting. Through analysis of the amplitudes and phase parameters of the received Lamb waves signals, the imaging is performed in a polar coordinate system where each pixel can be defined with its angular position and the distance from the center.

Total focusing method (TFM), also named as delay-and-sum algorithm, is processed with the amplitude information of signals. Using steered and possibly focused beam improves angular resolution in ultrasonic image but it requires scanning of the full structure. It is sensitive to the wavefield profile, signal-to-noise ratio (SNR), and the dispersion nature of Lamb waves [31]. Meanwhile, TFM suffers from large side lobes that result from overlapping echoes that result in the back-propagation. Adaptive imaging methods [32], where the weights are adjusted for each pixel, can offer a significant improvement to the side lobe behavior of TFM. Vector total focusing method, phase coherence factor (PCF), and the sign coherence factor (SCF) use signal phase information to perform the correction action and defect location. Besides achieving the main goal, these methods obtain improvements in lateral resolution and SNR. Implementation of the SCF technique is quite straight forward, operating in real-time, and can be added to any virtually existing beam former to improve the resolution [33]. Compared with amplitude-based imaging techniques, such as the TFM, the phase information-based techniques are no sensitive to Lamb waves dispersion. For enhancing the defect imaging performance, many imaging combination strategies are proposed, including the combination of the TFM and various polarity images or SCF for enhancing damage detection [34–36], the combination of the TFM, and the multiapodization polarity (MAP) technique [36, 37]. The formulas of the TFM and the SCF algorithms are expressed in Eqs. (13) and (14), respectively.

$$I_{TFM}(x,y) = \frac{1}{N^2}\sum_{i=1}^{N}\sum_{J=1}^{N} a_{ij}u_{ij}\left(\tau_{ij}(x,y)\right), \tag{13}$$

where N is the number of a linear array, a_{ij} corresponds to an apodization applied to individual elements to control some characteristics of the acoustic beam, such as main lobe width and side lobe levels, $u_{ij}(t)$ is the amplitude time domain data from all transmitter and receiver j; $\tau_{ij}(x, y)$ is the ToF from the transmitter i to the receiver j and passes the point (x, y).

$$I_{SCF}(x,z) = 1-\sigma, \quad \sigma^2 = 1-\left[\frac{1}{N^2}\sum_{i=1}^{N}\sum_{J=1}^{N} b_{ij}\left(\tau_{ij}(x,z)\right)\right]^2, \quad b_{ij}(t) = \begin{cases} -1 & , if \;\; v_{ij}(t) < 0 \\ 1 & , if \;\; v_{ij}(t) \geq 0 \end{cases}, \tag{14}$$

where σ is the standard deviation of the polarity $b_{ij}(t)$ of the aperture data; $b_{ij}(t)$ is the polarity or algebraic sign of the aperture data.

Minimum variance distortionless response (MVDR), also known as Capon's method, divides the signals into several subspaces. It can minimize the mean output power of the noise and interference. Their weights are determined by finding the vector to suppress undesired modes and incident angles [38]. One challenge associated with MVDR imaging is sensitive to the assumed look direction, which depends upon possibly unknown scattering characteristics [33]. Through adding a diagonal loading term, $\alpha\mathbf{I}$, to $\widehat{\mathbf{S}}\ (\omega)$, to obtain a non-singular $\widehat{\mathbf{S}}\ (\omega)$, in which α is proportional to the power of the received signals [39]. The incident angle and wavenumber of

http://dx.doi.org/10.5772/intechopen.79475

the signals are acquired through searching an array steering vectors that is orthogonal to the noise subspace. The MUSIC algorithm can provide the location or the direction-of-arrival of the active sources in the field with its high spatial resolution capability. Han et al. [40] used the time-frequency MUSIC [41] beamforming procedure to eliminate the effects of the direct excitation signals and the boundary-reflected wave signals. It is better than TFM for adjacent defect imaging when the signal-to-noise ratio is lower than 20dB [42]. **Figure 5** plots the comparison of the flow chart of the MVDR and the MUSIC algorithm.

Decomposition of the time-reversal operator (DORT) refocuses the wave energy back on multiple scatters, even for those that are neither small nor perfectly resolved. The whole DORT process is described in detail in Ref. [43]. DORT algorithm has the capability of individually imaging these scatters by back-propagating the eigenvectors obtained from eigenvalue decomposition of the time-reversal operator, providing separate information about each scatterer. When the scatterers are relatively large compared to the excitation wavelength, a single scatterer may generate multiple significant eigenvalues. In this case, the back-propagation of the eigenvectors can provide a certain amount of information about the relatively large scatterers. Time-reversal multiple signal classification algorithm was originally proposed by Schmidt [44]. Lehman and Devaney [45] developed a combined DORT and MUSIC algorithm, termed DORT-MUSIC, to image multiple buried cylinders in the seismo-acoustic application. He et al. [46] adopted the DORT-MUSIC in space-frequency domain for separating imaging from both the actuator-to-damage and the sensor-to-damage. The dispersion, multimode, and multireflection nature of Lamb waves have serious influence on the imaging performance of DORT, MUSIC, and DORT-MUSIC.

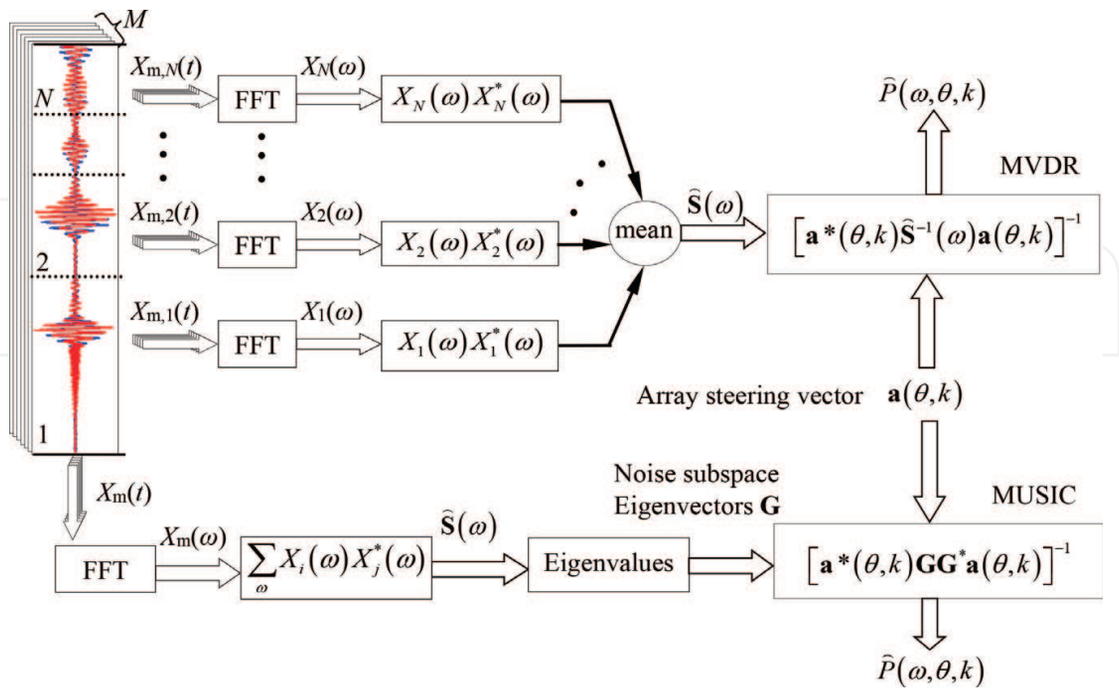

Figure 5. Comparison of the flow chart of the MVDR and the MUSIC algorithm.

Synthetic aperture focusing technique (SAFT) focuses the acoustic field along the 1D linear array toward the location of scatterer based on the angular and the distance information. It is first proposed for body waves defect detection. Sicard et al. [47] presented an F-SAFT algorithm for Lamb waves imaging in which the dispersion nature of Lamb waves is considered. Furthermore, multidefects detection in an isotropic plate was realized. Other algorithms for far-field defect imaging based on the wavenumber analysis have the spatial-wavenumber filter (SWF) [48–50] and wavenumber filtering algorithm [51]. Ren and Qiu [49, 52] proposed a scanning spatial-wavenumber filter-based diagnostic imaging method for online characterization of multi-impact event. The procession does not rely on any modeled or measured wavenumber response. The formulae of SCFT and the SWF are expressed as Eqs. (15)–(18), respectively.

$$I_{\mathrm{SCFT}}(x,d) = ifft\left(\sum_{f\in\Omega} s(k_x,d,f)\right),\quad s(k_x,d,f) = fft(u(x,t))\exp\left(2\pi di\sqrt{\frac{f^2}{\left(c_p(f\times 2h)/2\right)^2}-k_x^2}\right), \tag{15}$$

$$I_{\mathrm{SWF}}(k,t_r) = \sum\left|u(x,t_r)\otimes\phi(x)\right| = \sum\left|4\pi^2 A(t_r)\delta(k-k_a\cos\theta_a)\delta(k-k_a\cos\theta)\right|, \tag{16}$$

$$A(t_r) = u(t_r)e^{i\omega t_r}e^{-ik_a l_a}, \tag{17}$$

$$\phi(x) = \left[e^{ik_a x_1\cos\theta}, e^{ik_a x_2\cos\theta}, \ldots, e^{ik_a x_m\cos\theta}, \ldots, e^{ik_a x_M\cos\theta}\right], \tag{18}$$

where I_{SCFT} is the imaging result of SAFT, $u(x,t)$ is the spatial response acquired by the linear array, d is the propagation distance, k_x is the wavenumber in x direction; I_{SWF} is the imaging result of the SWF, $u(x,t_{\mathrm{r}})$ is the response acquired at time t_r, $\otimes$ indicates the convolution operation, $\phi(x)$ is the original spatial-wavenumber filter, a is the number of the transducer, θ_a, l_a are the angle and the distance of the damage respectively, k_a is the wavenumber at direction θ_a.

2.4. Full wavefield imaging techniques

With the aid of the laser ultrasonic system, the strategy used for capturing the full propagation wavefield relies on experiment settings in which one transducer at a fixed position and the second transducer as a movable point, actuator-sensor synchronization and signal registration at one point, in a repetitive manner at various locations. The time delay is introduced between consecutive wave excitations in order to wait until the wave fully attenuates. Researchers adopted the compressive sensing algorithm [53, 54] or combined binary search and compressed sensing [55] to improve the efficiency of full wavefield data acquisition. Once time-space wavefield data are acquired, data analysis can be implemented in time-space domain and frequency-wavenumber domain. The original signal process techniques are used for studying the amplitude information to observe the wave reflection with the root mean square and cumulative kinetic energy methods. Moreover, advanced signal processing techniques with 2D Fourier transform [44], such as wavenumber filtering, frequency-wavenumber analysis, space-frequency-wavenumber analysis, local wavenumber domain analysis, give the possibility

of damage size estimation [56, 57]. Mode separation can be performed similarly for reflection separation [58].

The imaging techniques based on time-domain signal process have the integral mean value (IMV), the root mean square (RMS), and the weighted root mean square (WRMS) [59] that can be expressed as Eqs. (19)–(22), respectively.

$$\mathrm{IMV}(u(t)) = \frac{1}{t_2 - t_1}\int_{t_1}^{t_2} u(t)dt \approx \frac{1}{n}\sum_{k=1}^{n} u_k, \tag{19}$$

$$\mathrm{RMS}(u(t)) = \sqrt{\frac{1}{t_2 - t_1}\int_{t_1}^{t_2}\left[u(t)^2\right]dt} \approx \sqrt{\frac{1}{n}\sum_{k=1}^{n}\left[u_k^2\right]}, \tag{20}$$

$$\mathrm{WRMS}(u(t)) = \sqrt{\frac{1}{t_2 - t_1}\int_{t_1}^{t_2}\left[w(t)u(t)^2\right]dt} \approx \sqrt{\frac{1}{n}\sum_{k=1}^{n}\left[w_k u_k^2\right]}, \tag{21}$$

$$w_k = w(t_k) = k^m, m \geq 0 \tag{22}$$

where $u(t)$ is the received signals at n points. For a discrete signal u_r=$u(t_r)$ sampled at n points with time intervals Δt, following relation can be written as u_k=$u(t_k)$, t_k=t_1+(k-1)Δt, Δt=(t_2-t_1)/(n-1), k=1,2,…,n. $w(t)$ is a weighting factor, which decreases the importance of the time samples closer to the beginning of the sampling process and increases the importance of the samples closer to its end. t_1 and t_2 denote the beginning and the end of the sampling process, respectively. The weighting factor w_k=k (m=1), the importance (weight) of particular time samples, increases linearly with time t; this importance (weight) increases as a square function of time t when the weighting factor is w_k=k^2 (m=2).

The effectiveness of the applied algorithms is strongly dependent on the calculation parameters (weighting factor and time window), excitation frequency, and damage types. The extension of the time window leads to the increase in differences in the WRMS values between the damaged and undamaged areas. The constant weighting factors do not provide efficient results due to the high influence of the incident wave at excitation point. The statistical analysis of the calculated WRMS values was adopted to successfully supplement the visual assessment of the defect imaging [60].

The multidimensional Fourier transform maps the time-space domain signals into the frequency-wavenumber domain and realizes defect imaging; the formula of the transform can be expressed as

$$I(\omega, k_x, k_y) = \int_{-\infty}^{\infty}\int_{-\infty}^{\infty}\int_{-\infty}^{\infty} u(x, y, t)W(x - a, y - b)e^{-i\left(\omega t + k_x x + k_y y\right)}dydxdt, \tag{23}$$

where $u(x,y,t)$ is the full wavefield data; a and b are the coordinates of the window function in x and y dimension; W is the window with various of types, including rectangle window, Gauss window, and Hanning window. For a Hanning window with a diameter of D_r, W can be expressed as

$$W(x,y) = \begin{cases} 0.5\left[1-\cos\left(2\pi\dfrac{\sqrt{x^2+y^2}}{D_r}\right)\right] & if\ \sqrt{x^2+y^2} \le 0.5D_r \\ 0 & \text{otherwise} \end{cases}. \tag{24}$$

The wavenumber adaptive image filtering is introduced in reference [61] and further expanded in reference [62] in which the data are transformed from Cartesian coordinates to polar coordinates. In the frequency-wavenumber domain, the filtering is applied to separate the different modes or forward and backward waves, as shown in Eq. (25).

$$\tilde{S}(\omega, k_r; \theta_i) = I(\omega, k_r; \theta_i) W(k_r, \omega), \tag{25}$$

where $\tilde{S}(\omega, k_r; \theta_l)$ is the separating waves in frequency-wavenumber domain, $I(\omega,k_r;\theta_i)$ is the frequency-wavenumber result of the $u(t,r;\theta)$ in polar coordinates; θ_i is the specific angle index; $W(k_r,\omega)$ is a 2D window function operating as a filter in frequency-wavenumber domain.

Finally, the filtered data are successively transformed back to the time domain in polar coordinates and Cartesian coordinates.

Harley et al. [63] presented a baseline-free, model-driven, statistical damage detection, and imaging framework for guided waves measured from partial wavefield scans in which the sparse wavenumber analysis, sparse wavenumber synthesis, and data-fitting optimization to accurately model damage-free wavefield data. Kudela et al. [64] combined the time-distance mapping technique and novel Lamb waves focusing technique to realize crack detection. Meanwhile, the temperature effect is compensated by using the temperature-dependent dispersion curve. Pai et al. [65] presented a dynamics-based methodology for accurate damage inspection of thin-walled structures by combining a boundary effect evaluation method for space-wavenumber analysis of measured operational deflection shapes and a conjugate-pair decomposition method for time-frequency analysis of time traces of measured points. Li et al. [66] proposed a correlation filtering-based matching pursuit signal processing approach to realize precise value of time of flight and locating and sizing the delamination in composite beams. Through analysis, the reflection intensity of Lamb waves from an elliptical damage realized defect sizing [67]. Perelli et al. [68] combined the wavelet packet transform and frequency warping to generate a sparse decomposition of the acquired dispersive signal. Tofeldt et al. [69] presented a 2D array and wide-frequency bandwidth technique for Lamb waves phase velocity imaging. Through a discrete Fourier transform, a spectral estimate is obtained for the 2D array in the frequency-phase velocity domain. The variation of the phase velocity is then mapped using a stepwise movement of the 2D array within the complete measurement domain.

3. Intelligent recognition techniques

There are mainly two steps for defect recognition in structure integrity evaluation, i.e., feature extraction and classifier design. Time-frequency and time-scale analysis techniques

http://dx.doi.org/10.5772/intechopen.79475

are adopted for feature extraction, including dynamic wavelet fingerprinting, wavelet transform (CWT, DWT, and wavelet packet decomposition), and statistical features [70]. While the processing of the feature extraction with these techniques may be very time consuming [71] and cannot ensure the feature data are optimally suitable for mapping the state of structures. Additionally, overtrain may be induced with the available dataset for these methods. So, many techniques have been developed to optimize the feature extraction process. The principal component analysis (PCA) is one of the most widely used linear mapping techniques for feature reduction [72, 73]. Nonlinear mapping techniques reduce dimensionality following the criterion which minimizes the difference between interpoint distances of the initial and detection/monitoring feature space, including Sammon mapping, self-organizing maps, and the generative topographic maps [74]. In the following part of this section, we focus on the introduction of the pattern recognition model that attracted relatively more attention in structure integrity evaluation, such as support vector machine, Bayesian methodology, and neural networks.

3.1. Support vector machine

Support vector machine (SVM) is a supervised learning classifier that uses a kernel function to form a hypothesis space in a high-dimensional feature space for linear and nonlinear classification. The principle schematic diagram of support vector machine is plotted in **Figure 6**. The kernel function may be a linear, polynomial, sigmoid, or custom kernels. Given a set of training examples that are belonging to two categories, an SVM training algorithm builds a model that assigns the examples to one category or the other. In this case, the SVM is a nonprobabilistic binary linear classifier that is not common in practical application. For nonlinear classification and regression problems, the input data are mapped to another linearly separable space using a nonlinear kernel function ϕ and the normal linear SVM. The least squares support vector machine (LS-SVM) is an improved variant of SVM. It can increase the convergence rate for complex problems [75]. The general formula of the LS-SVM can be expressed as

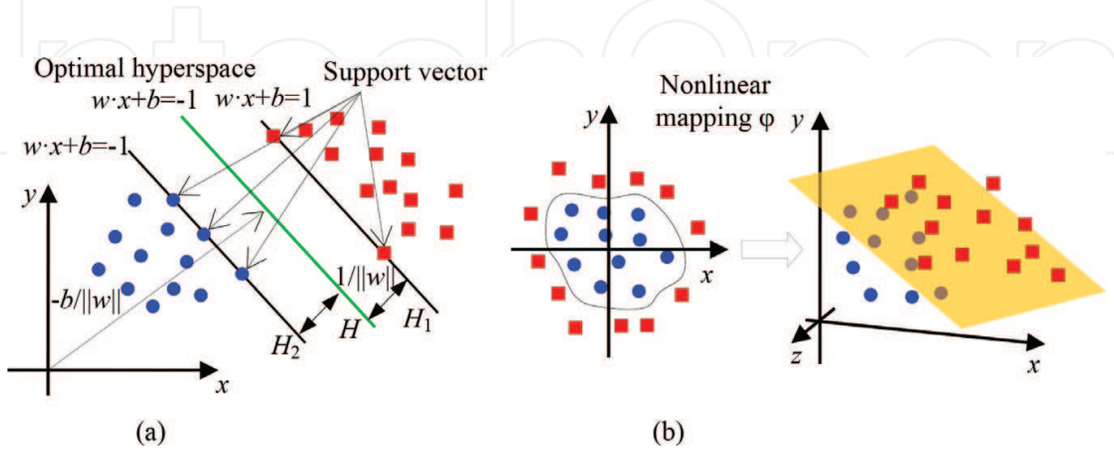

Figure 6. Principle schematic diagram of support vector machine. (a) Linearly separable space with linear function and (b) linearly separable space with nonlinear function.

$$y(x) = w^T \phi(x) + b, \tag{26}$$

where the term $\phi(\cdot)$ is a nonlinear mapping function, $w \in R^n$ and $b \in R$ are the mode parameters.

SVM is a robust classifier in the existence of noise and more computational efficient than artificial neural network (ANN) [76]. Das et al. [77] developed an one-class SVM algorithm to characterize and classify different damage states in composite laminates by measuring the change in the signature of the Lamb waves that propagates through the anisotropic media under forced excitations. Park et al. [78] used SVM to enhance the damage identification with the extracted damage features. In the study, multifeatures were extracted for mapping the state of structures, including TOF, the root mean square deviations (RMSD) of the impedances, and wavelet coefficients (WC) of Lamb waves. Then, in Ref. [79], the same authors proposed a two-step support vector machine (SVM) classifier for railroad track damage identification that forms optimal separable hyperplanes. In the study, a two-dimensional damage feature space was built with the root mean square deviations (RMSD) of impedance signatures and the sum of square of wavelet coefficients for maximum energy mode of guided waves. In the process, the damage detection was accomplished by the first step-SVM, and damage classification was carried out by the second step-SVM. Sun et al. [80] adopted genetic algorithm to optimize the LS-SVM parameters in which normalized amplitude, phase change, and correlation coefficient were proposed to build the damage features.

3.2. Bayesian methodology

The Bayes' theorem combines a prior belief and the observation regarding the related parameters through the likelihood function to update the distribution of the interested parameters in which the model parameters u can be updated using the observation data θ, as expressed as

$$q(u) \propto p(u)p(\theta|u), \tag{27}$$

where $p(u)$ is the prior distribution of the model parameters u that can be a vector for multiple parameters. $p(\theta|u)$ is the likelihood function. $q(u)$ is the posterior distribution of updated parameter u.

$$q(\theta|x_1, x_2, \ldots, x_n) \propto p(\theta)\left(\frac{1}{\sqrt{2\pi}\sigma_\varepsilon}\right)^n \times \exp\left\{-\frac{1}{2}\sum_{i=1}^{n}\left[\frac{x_i - M(\theta)}{\sigma_\varepsilon}\right]^2\right\}, \tag{28}$$

where $M(\theta)$ is a parameterized model describing the relationship between the signal features and damage information. σ_ε is the standard deviation of the error term. The posterior distribution of each parameter is estimated by the samples generated with the Markov-Chain Monte-Carlo method.

Bayesian methodology is a probabilistic detection technique that has the ability to consider the uncertainties such as measurement uncertainty, and model parameter uncertainty in damage

http://dx.doi.org/10.5772/intechopen.79475

detection/monitoring. A multivariate regression model is proposed to correlate damage features, the phase change, and normalized amplitude, to the actual crack size [81]. It is a baseline crack size quantification model can also use for more general and complex structures. Prior distributions of model parameters are obtained using the coupon test data. The posterior distribution of the parameters and the posterior distribution of θ in a multivariate regression model are expressed as Eq. (28). A multilevel Bayesian framework is proposed for identifying the position and the effective mechanical properties of the damaged layers in composite laminates [82] in which the framework is initially applied to a set of synthetic signals with increasing levels of noise and complexity. He et al. [83] employed the Bayesian model to determine the crack number, and then, the Bayesian statistical framework was used to identify the crack parameters and the associated uncertainties in beam-like structures. The proposed method is able to accurately identify the number, locations, and sizes of the cracks, and is robust under measurement noise.

Bayesian imaging method (BIM) is used to build the likelihood function using the differences between the model predictions and the field observations. The structure is discretized into many small cells, and each cell is assigned an associated probability of damage, such as the location and size. Next, the overall posterior distribution of the parameters can be obtained by combining the prior information about the parameters. The marginal posterior distribution of each parameter is estimated by the samples generated using the Markov-Chain Monte-Carlo method. Given the parameter samples, the probability of damage in each cell is computed using the ratio of the number of samples falling into each cell to the total number of samples. Following the damage probability distribution can be used to construct an image that directly represents the damage location and size. Peng et al. [84] presented a Bayesian imaging technique to simultaneously estimate damage location and size, as well as the corresponding uncertainty bounds. Neerukatti et al. [85] used a sequential Bayesian technique to combine a physics-based damage prognosis model with a data-driven probabilistic damage localization approach for effective damage localization and prognosis in complex metallic structures. Sohn et al. [86] proposed an instantaneous damage diagnosis based on the concepts of time reversal acoustics and consecutive outlier analysis to minimize damage misclassification without relying on past baseline data.

Gaussian mixture model (GMM) is a probability static method for characterizing uncertainties based on unsupervised learning. This method organizes itself according to the nature of the input data with probability distributions without any prior knowledge. The GMM has the advantages of better robustness of uncertainties and high efficiency with lower computational complexity with a relatively small number of model parameters. PCA is used to reduce the dimensions of the extracted multistatistical characteristic parameters of the excited Lamb waves, then training the damage identification system using the GMM [73]. Several statistical characteristic parameters, including the root mean square (RMS), variance, skewness, kurtosis, peak-to-peak (PPK), and K-factor, are extracted as the input for the GMM-processed Lamb wave-based identification model. Qiu et al. [72] proposed an online updating Gaussian mixture model (GMM), for aircraft wings par damage evaluation under time-varying boundary conditions in which the formulas are expressed as Eqs. (29) and (30).

$$\phi(f_r|\boldsymbol{\mu},\boldsymbol{\Sigma}) = \sum_{i=1}^{C} w_i \phi_i(f_r|\boldsymbol{\mu}_i,\boldsymbol{\Sigma}_i), \tag{29}$$

$$\phi_i(f_r|\boldsymbol{\mu}_i,\boldsymbol{\Sigma}_i) = \frac{1}{(2\pi)^{d/2}} \exp\left\{-\frac{1}{2}(f_r-\boldsymbol{\mu}_i)^T \sum_i^{-1}(f_r-\boldsymbol{\mu}_i)\right\}, \tag{30}$$

where $f=\{f_1,f_2,\ldots,f_k\}$ is a random sample set composed by k independent random samples. f_r denotes a d-dimensional sample in the sample set, where $f_r=\{f_1,f_2,\ldots,f_d\}^T$ and $r=1,2,\ldots,k$, $\boldsymbol{\mu}_i$, Σ_i and w_i are the mean, the covariance matrix and the mixture weight of the i^{th} Gaussian component, respectively, and $i=1,2,\ldots C$, C is the number of Gaussian components, $\phi_i(f_r|\boldsymbol{\mu}_i, \Sigma_i)$ is the probability density of each Gaussian component is a d-dimensional Gaussian function.

3.3. Neural networks

Neutral network is comprised of layouts that are built with artificial neurons, termed nodes. These nodes in the adjacent layers are connected to each other with various of strengths (weights). The high weights value indicates a strong connection; vice versa, it is a weak connection. **Figure 7** shows the principle diagram of a three-layer neutral network in which the three-layer neural

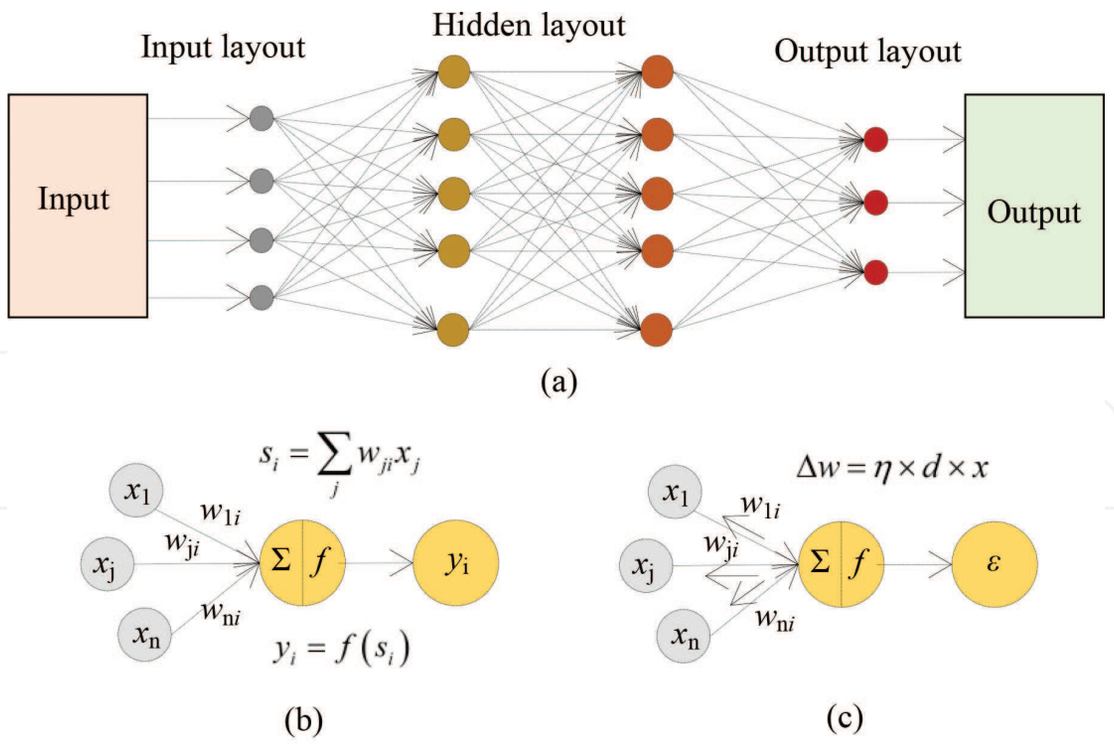

Figure 7. Principle diagram of a three-layer neural network. (a) Three-layer neural network, (b) forward, and (c) backward.

http://dx.doi.org/10.5772/intechopen.79475

network, the forward and the backward principles are plotted in **Figure 7(a)**, **(b)** and **(c)**, respectively. There exists three types of nodes including input nodes, hidden nodes, and output nodes. Except the input layer out, there is a transfer function in each node to transfer input data to the connected nodes in the adjacent layout. The typical transfer function used in a neural network classifier has the unit step (threshold), sigmoid, piecewise linear, and Gaussian. The training of neutral networks consists of the forward propagation and the backward propagation. In the forward propagation process, the input nodes take the feature date into the model. The information is presented as activation values, where each node is given a value, the higher value, the greater activation. Based on the weights, inhibition or excitation, and transfer functions, the activation value is passed from node to node. The activation values at each node are summed. Then, the value is modified based on its transfer function. The activation flows through the network, through hidden layers, until it reaches the output nodes. Then, the difference between the output value and actual value (error) modified with the backward propagation process with gradient descent algorithm until satisfy a stop threshold. The diagnostic efficiency and precision are highly dependent on the network architecture [87]. The traditional artificial neural networks (ANNs) have been adopted in defect recognition such as welding defects [88], delamination in composite structures [89], and composite plates structural health monitoring [90]. De Fenza et al. [91] combined the ANN and the probability ellipse method to determine the location and degree of defects in aluminum and composite plates.

Benefiting from the flexible configuration of neural networks, researcher developed many kinds of neural networks used in structure integrity evaluation. Probabilistic neural network (PNN) combines the Bayes decision strategy with the Parzen nonparametric estimator of the probability density functions in which the interpretation of the neural network is in the form of a probability density function. An accepted norm for decision strategies used to classify patterns is that they minimize the "expected risk." Park et al. [92] adopted the PNN and SVM to online monitoring the state of jointed plates in which the extracted damage feature that constructed with the ToF and the wavelet coefficient obtained from wavelet transforms of Lamb wave signals. Kohonen neural network (KNN) has two layers, input layer and output layer, and is used for honeycomb sandwich and carbon fiber composite structures studied in which the amount of neuron in input layer is determined by input vector dimensions [93]. The neurons of output layer layout form a 2D plane. In regression neural networks for pattern recognition, a trained network produces large errors when some parts of the test pattern are not found in the training pattern. The weight-range selection (WRS) method has a supervised multilayer perceptron operating with one hidden layer of neurons and trained using a back-propagation algorithm to eliminate the large errors induced by the case a test pattern not found in the training set [94]. Anaya et al. [95] adopted an artificial immune system (AIS) and the notion of affinity was used for the sake of damage detection and used a fuzzy *c*-means algorithm is used for damage classification of an aircraft skin panel. Compared with standard Lamb waves based methods, there is no need to directly analyze the complex time-domain traces containing overlapping, multimodal, and dispersive wave propagation. Other kinds of neural networks that have been studied in nondestructive testing have the recurrent neural network (RNN) [96], deep learning network (DLN), and convolutional neural network (CNN).

4. Summary and conclusions

In this chapter, we divided the defects imaging techniques into four categories based on the setting of detection/monitoring system, and the basic principle of them is introduced. Three kinds of intelligent recognition techniques that have been widely studied in Lamb waves structural integrity evaluation are also reviewed.

1. The discrete ellipse imaging algorithm, the hyperbola imaging technique, and the tomography imagine algorithms are processed in the detection/monitoring based on sparse arrays in which the spacing between the adjacent transducers is larger than the wavelength. Discrete ellipse imaging, the hyperbola imaging algorithm, and their optimal type are processed with the defect scattering signals. The pixel intensity is drawn in an elliptical trajectory and the hyperbola trajectory, respectively. Both of the algorithms are imaging with the amplitude information and sensitive to the dispersion and the SNR of signals. The imaging performance is closely related with transducer numbers and the signal resolutions. In the tomography technique, the distribution of sensing points has relative regular forms such as the parallel, square, or circular. The imaging algorithms used in the tomography have PRA algorithms, FBP-based algorithm, the ART-based algorithms, and the novel algorithms such as the HARBUT and FWI. With the dense ray in the detection, defect sizing can be realized with the tomography techniques, particularly for the HARBUT, and FWI has attractive performance in accuracy corrosion defect imaging.

2. Compact array in which the spacing of the adjacent transducers is shorter than the wavelength that with various of shapes have been developed in Lamb waves based defects imaging, including 1D linear array, 2D rectangular, circular, and spiral arrays. The defect imaging algorithms based on compact arrays have PA, SA, and the full wavefield techniques. The TFM, SCF, MVDR, MUSIC, SAFT-based imaging algorithms, and the SWF can be used for full-scale scanning of the plate and realizing defect location. The TFM is an imaging algorithm with the amplitude information that is sensitive to the dispersion nature of Lamb waves. The phase information-based algorithms, PCF, SCF, have relatively more robust imaging performance than TFM. Besides these algorithms, MVDR, MUSIC, SAFT, and SWF have the potential used for baseline-free detection. The full wavefield techniques have the ability for defect accuracy imaging by analyzing the received full wavefield data. Among them, the IMV, RMS, and WRMS are adopted to time-domain analysis for defect location and sizing. With the 2D Fourier transform, the received time-space data are mapped into frequency-wavenumber domain, and defect sizing and thinning quantification are realized through analysis of the spatial wavenumber information. Meanwhile, many optimization techniques with the added windows are adopted to separate the scattering waves in frequency-wavenumber domain for reflection waves separation, defect imaging can be enhanced.

3. SVM, Bayesian methodology, and the neural networks are three kinds of typical classifiers used in Lamb waves based structure integrity evaluation. SVM maps the input data that indicates the state of the structures into a hypothesis space with a kernel function that may be a linear, polynomial, or custom kernel. The classifiers based on SVM have the one-class

SVM, LS-SVM, two-step SVM. Bayesian methodology realizes the observation of data estimation with the prior received data. For the Bayesian methodology, the state of structures is predicated with the prior distributions of model parameters obtained using the coupon test data. The related techniques have the multilevel Bayesian model, Bayesian imaging method, and the GMM. Among them, the GMM is a probability static method with unsupervised learning property. It has the advantages of better robustness of uncertainties and high efficiency with lower computational complexity with a relatively small number of model parameters. Neural networks are a supervise classifier based on the back-propagation algorithm to optimize the model parameters. Benefiting from the flexible configuration of neural networks, researchers developed many kinds of neural networks for structure integrity evaluation. During the past decade, ANN, PNN, KNN, CNN, etc., have been applied for on- or offline structure integrity evaluation with the extracted Lamb waves defect information. These neural networks can realize accurate defect recognition in the case they are trained with enough dataset. Meanwhile, they have low noise tolerance in field applications.

Acknowledgements

This work was supported by the National Natural Science Foundation of China (Grant Nos. 51475012, 11772014, 11527801, and 11272021).

Conflict of interest

We declare that we do not have any commercial or associative interest that represents a conflict of interest in connection with the work submitted.

Author details

Zenghua Liu* and Honglei Chen

*Address all correspondence to: liuzenghua@bjut.edu.cn

College of Mechanical Engineering and Applied Electronics Technology, Beijing University of Technology, Beijing, China

References

[1] Liu ZH, Yu FX, Wei R, He CF, Wu B. Image fusion based on single-frequency guided wave mode signals for structural health monitoring in composite plates. Materials Evaluation. 2013;**71**:1434-1443

[2] Muller A, Robertson-welsh B, Gaydecki P, Gresil M, Soutis C. Structural health monitoring using Lamb wave reflections and total focusing method for image reconstruction. Applied Composite Materials. 2017;**24**:553-573. DOI: 10.1007/s10443-016-9549-5

[3] Croxford AJ, Wilcox PD, Drinkwater BW, Konstantinidis G. Strategies for guided-wave structural health monitoring. Proceedings of the Royal Society A: Mathematical Physical and Engineering Sciences. 2007;**463**:2961-2981

[4] Michaels JE, Michaels TE. Guided wave signal processing and image fusion for in situ damage localization in plates. Wave Motion. 2007;**44**:482-492. DOI: 10.1016/j.wavemoti.2007.02.008

[5] Shan SB, Qiu JH, Zhang C, Ji HL, Cheng L. Multi-damage localization on large complex structures through an extended delay-and-sum based method. Structural Health Monitoring. 2016;**15**:50-64. DOI: 10.1177/1475921715623358

[6] Michaels JE. Detection, localization and characterization of damage in plates with an in situ array of spatially distributed ultrasonic sensors. Smart Materials and Structures. 2008;**17**:35035. DOI: 10.1088/0964-1726/17/3/035035

[7] Flynn EB, Todd MD, Wilcox PD, Drinkwater BW, Croxford AJ. Maximum-likelihood estimation of damage location in guided-wave structural health monitoring. Proceedings of the Royal Society A: Mathematical Physical and Engineering Sciences. 2011;**467**:2575-2596. DOI: 10.1098/rspa.2011.0095

[8] Gao DY, Wu ZJ, Yang L, Zheng YB. Guide waves-based multi-damage identification using a local probability-based diagnostic imaging method. Smart Materials and Structures. 2016;**25**:45009. DOI: 10.1088/0964-1726/25/4/045009

[9] Leonard KR, Malyarenko EV, Hinders MK. Ultrasonic Lamb wave tomography. Inverse Problems. 2002;**18**:1795-1808. DOI: 10.1088/0266-5611/18/6/322

[10] Liu ZH, Yu HT, Fan JW, Hu YN, He CF, Wu B. Baseline-free delamination inspection in composite plates by synthesizing noncontact air-coupled Lamb wave scan method and virtual time reversal algorithm. Smart Materials and Structures. 2015;**24**. DOI: 10.1088/0964-1726/24/4/045014

[11] Liu ZH, Zhong XW, Dong TC, He CF, Wu B. Delamination detection in composite plates by synthesizing time-reversed Lamb waves and a modified damage imaging algorithm based on RAPID. Structural Control and Health Monitoring. 2017;**24**:1-17. DOI: 10.1002/stc.1919

[12] Lee J, Sheen B, Cho Y. Multi-defect tomographic imaging with a variable shape factor for the RAPID algorithm. Journal of Visualization. 2016;**19**:393-402. DOI: 10.1007/s12650-015-0290-1

[13] Lee J, Sheen B, Cho Y. Quantitative tomographic visualization for irregular shape defects by guided wave long range inspection. International Journal of Precision Engineering and Manufacturing. 2015;**16**:1949-1954. DOI: 10.1007/s12541-015-0253-4

[14] Keulen CJ, Yildiz M, Suleman A. Damage detection of composite plates by Lamb wave ultrasonic tomography with a sparse hexagonal network using damage progression trends. Shock and Vibration. 2014;**2014**:1-8. DOI: 10.1155/2014/949671

[15] Sheen B, Cho Y. A study on quantitative Lamb wave tomogram via modified RAPID algorithm with shape factor optimization. International Journal of Precision Engineering and Manufacturing. 2012;**13**:671-677. DOI: 10.1007/s12541-012-0087-2

[16] Zhao XL, Gao HD, Zhang GF, Ayhan B, Yan F, Kwan C, Rose JL. Active health monitoring of an aircraft wing with embedded piezoelectric sensor/actuator network: I. Defect detection, localization and growth monitoring. Smart Materials and Structures. 2007;**16**:1208-1217. DOI: 10.1088/0964-1726/16/4/032

[17] Torkamani S, Roy S, Barkey ME, Sazonov E, Burkett S, Kotru S. A novel damage index for damage identification using guided waves with application in laminated composites. Smart Materials and Structures. 2014;**23**. DOI: 10.1088/0964-1726/23/9/095015

[18] Wright W, Hutchins D, Jansen D, Schindel D. Air-coupled Lamb wave tomography. IEEE Transactions on Ultrasonics, Ferroelectrics, and Frequency Control. 1997;**44**:53-59. DOI: 10.1109/58.585190

[19] Mokhtari AA, Ohadi A, Amindavar H. Polygonal damage shape reconstruction in plates using guided Lamb wave. Structural Control and Health Monitoring. 2017;**24**:e1907. DOI: 10.1002/stc.1907

[20] Nagata Y, Huang J, Achenbach JD, Krishnaswamy S. Lamb wave tomography using laser-based ultrasonics. In: Proceedings of the Annual Review of Progress in Quantitative Nondestructive Evaluation; 31 July–04 August 1994; Snowmass Village. New York: Plenum Press Div Plenum Publishing Corp; 1995. pp. 561-568

[21] Ladas KT, Devaney AJ. Generalized ART algorithm for diffraction tomography. Inverse Problems. 1991;**7**:109-125. DOI: 10.1088/0266-5611/7/1/011

[22] Wang DJ, Zhang WF, Wang XY, Sun B. Lamb-wave-based tomographic imaging techniques for hole-edge corrosion monitoring in plate structures. Materials. 2016;**9**:916. DOI: 10.3390/ma9110916

[23] Prasad SM, Balasubramaniam K, Krishnamurthy CV. Structural health monitoring of composite structures using Lamb wave tomography. Smart Materials and Structures. 2004;**13**:N73-N79. DOI: 10.1088/0964-1726/13/5/N01

[24] Malyarenko EV, Hinders MK. Ultrasonic Lamb wave diffraction tomography. Ultrasonics. 2001;**39**:269-281. DOI: 10.1016/S0041-624X(01)00055-5

[25] Miller CA, Hinders MK. Classification of flaw severity using pattern recognition for guided wave-based structural health monitoring. Ultrasonics. 2014;**54**:247-258. DOI: 10.1016/j.ultras.2013.04.020

[26] Azimi M, Kak AC. Distortion in diffraction tomography caused by multiple scattering. IEEE Transactions on Medical Imaging. 1983;**2**:176-195. DOI: 10.1109/TMI.1983.4307637

[27] Huthwaite P, Simonetti F. High-resolution guided wave tomography. Wave Motion. 2013; **50**:979-993. DOI: 10.1016/j.wavemoti.2013.04.004

[28] Rao J, Ratassepp M, Fan Z. Guided wave tomography based on full waveform inversion. IEEE Transactions on Ultrasonics, Ferroelectrics, and Frequency Control. 2016;**63**:737-745. DOI: 10.1109/TUFFC.2016.2536144

[29] Rao J, Ratassepp M, Fan Z. Investigation of the reconstruction accuracy of guided wave tomography using full waveform inversion. Journal of Sound and Vibration. 2017;**400**: 317-328. DOI: 10.1016/j.jsv.2017.04.017

[30] Stepinski T, Ambrozinski L, Uhl T. Designing 2D arrays for SHM of planar structures: A review. In: Proceedings of the Conference on Nondestructive Characterization for Composite Materials, Aerospace Engineering, Civil Infrastructure, and Homeland Security; 11–14 March 2013; San Diego. Bellingham: SPIE Press; 2013. pp. 86941-86941

[31] Tian ZH, Leckey CAC, Yu LY. Phased array beamforming and imaging in composite laminates using guided waves. In: Proceedings of the SPIE Conference on Health Monitoring of Structural and Biological Systems; 21–24 March 2016; Las Vegas. Bellingham: SPIE Press; 2016. p. 980505

[32] Michaels JE, Michaels TE. Adaptive imaging of damage from changes in guided wave signals recorded from spatially distributed arrays. In: Proceedings of the Conference on Health Monitoring of Structural and Biological Systems, 8–12 March 2009, San Diego, California: SPIE Press; 2009, 7295: p. 729515. DOI:10.1117/12.815849

[33] Camacho J, Parrilla M, Fritsch C. Phase coherence imaging. IEEE Transactions on Ultrasonics, Ferroelectrics, and Frequency Control. 2009;**56**:74-958. DOI: 10.1109/TUFFC.2009.1128

[34] Liu ZH, Sun KM, Song GR, He CF, Wu B. Damage localization in aluminum plate with compact rectangular phased piezoelectric transducer array. Mechanical Systems and Signal Processing. 2016;**70-71**:625-636. DOI: 10.1016/j.ymssp.2015.09.022

[35] Prado VT, Higuti RT, Kitano C, Martinez-Graullera O, Adamowski JC. Lamb mode diversity imaging for non-destructive testing of plate-like structures. NDT&E International. 2013;**59**:86-95. DOI: 10.1016/j.ndteint.2013.06.001

[36] Higuti RT, Martinez-Graullera O, Martin CJ, Octavio A, Elvira L, de Espinosa FM. Damage characterization using guided-wave linear arrays and image compounding techniques. IEEE Transactions on Ultrasonics, Ferroelectrics, and Frequency Control. 2010;**57**:1985-1995. DOI: 10.1109/TUFFC.2010.1646

[37] Prado VT, Higuti RT, Kitano C, Martinez-Graullera Q. Sparse arrays and image compounding techniques for non-destructive testing using guided acoustic waves. Journal of Control Automation and Electrical Systems. 2013;**24**:263-271. DOI: 10.1007/s40313-013-0029-y

[38] Engholm M, Stepinski T. Direction of arrival estimation of Lamb waves using circular arrays. Structural Health Monitoring. 2011;**10**:467-480. DOI: 10.1177/1475921710379512

[39] Li J, Stoica P, Wang ZS. On robust capon beamforming and diagonal loading. IEEE Transactions on Signal Processing. 2003;**51**:1702-1715. DOI: 10.1109/TSP.2003.812831

[40] Han JH, Kim YJ. Time-frequency beamforming for nondestructive evaluations of plate using ultrasonic Lamb wave. Mechanical Systems and Signal Processing. 2015;**54-55**:336-356. DOI: 10.1016/j.ymssp.2014.09.008

[41] Belouchrani A, Amin MG. Time-frequency MUSIC. IEEE Signal Processing Letters. 1999; **6**:109-110. DOI: 10.1109/97.755429

[42] Fan CG, Caleap M, Pan MC, Drinkwater BW. A comparison between ultrasonic array beamforming and super resolution imaging algorithms for non-destructive evaluation. Ultrasonics. 2014;**54**:1842-1850. DOI: 10.1016/j.ultras.2013.12.012

[43] Prada C, Manneville S, Spoliansky D, Fink M. Decomposition of the time reversal operator: Detection and selective focusing on two scatterers. Journal of the Acoustical Society of America. 1996;**99**:2067-2076. DOI: 10.1121/1.415393

[44] Schmidt RO. Multiple emitter location and signal parameter estimation. IEEE Transactions on Antennas and Propagation. 1986;**34**:276-280. DOI: 10.1109/TAP.1986.1143830

[45] Lehman SK, Devaney AJ. Transmission mode time-reversal super-resolution imaging. Journal of the Acoustical Society of America. 2003;**113**:2742-2753. DOI: 10.1121/1.1566975

[46] He JZ, Yuan FG. Lamb wave-based subwavelength damage imaging using the DORT-MUSIC technique in metallic plates. Structural Health Monitoring. 2016;**15**:65-80. DOI: 10.1177/1475921715623359

[47] Sicard R, Goyette J, Zellouf D. A SAFT algorithm for Lamb wave imaging of isotropic plate-like structures. Ultrasonics. 2002;**39**:487-494. DOI: 10.1016/S0041-624X(01)00087-7

[48] Purekar AS, Pines DJ. Damage detection in thin composite laminates using piezoelectric phased sensor arrays and guided Lamb wave interrogation. Journal of Intelligent Material Systems and Structures. 2010;**21**:995-1010. DOI: 10.1177/1045389X10372003

[49] Qiu L, Liu B, Yuan SF, Su ZQ, Ren YQ. A scanning spatial-wavenumber filter and PZT 2-D cruciform array based on-line damage imaging method of composite structure. Sensors and Actuators A: Physical. 2016;**248**:62-72. DOI: 10.1016/j.sna.2016.04.062

[50] Ren YQ, Qiu L, Yuan SF, Bao Q. On-line multi-damage scanning spatial-wavenumber filter based imaging method for aircraft composite structure. Materials. 2017;**10**:519. DOI: 10.3390/ma10050519

[51] Yoo B, Pines DJ. A magnetostrictive phased array sensor using a nickel comb patch for guided Lamb wave-based damage detection. In: Proceedings of the Conference on Sensors and Smart Structures Technologies for Civil, Mechanical, and Aerospace Systems; 26–29 March 2017; Portland. Bellingham: SPIC; 2017. pp. 1-9

[52] Ren YQ, Qiu L, Yuan SF, Su ZQ. A diagnostic imaging approach for online characterization of multi-impact in aircraft composite structures based on a scanning spatial-wavenumber

filter of guided wave. Mechanical Systems and Signal Processing. 2017;**90**:44-63. DOI: 10.1016/j.ymssp.2016.12.005

[53] Esfandabadi YK, De Marchi L, Testoni N, Marzani A, Masetti G. Full wavefield analysis and damage imaging through compressive sensing in Lamb wave inspections. IEEE Transactions on Ultrasonics, Ferroelectrics, and Frequency Control. 2018;**65**:269-280. DOI: 10.1109/TUFFC.2017.2780901

[54] Mesnil O, Ruzzene M. Sparse wavefield reconstruction and source detection using compressed sensing. Ultrasonics. 2016;**67**:94-104. DOI: 10.1016/j.ultras.2015.12.014

[55] Park B, Sohn H, Liu PP. Accelerated noncontact laser ultrasonic scanning for damage detection using combined binary search and compressed sensing. Mechanical Systems and Signal Processing. 2017;**92**:315-333. DOI: 10.1016/j.ymssp.2017.01.035

[56] Tian ZH, Leckey C, Rogge M, Yu LY. Crack detection with Lamb wave wavenumber analysis. In: Proceedings of the Conference on Health Monitoring of Structural and Biological Systems; 11–14 Match 2013; San Diego. Bellingham: SPIE Press; 2013. p. 86952

[57] Yu LY, Tian ZH, Leckey CAC. Crack imaging and quantification in aluminum plates with guided wave wavenumber analysis methods. Ultrasonics. 2015;**62**:203-212. DOI: 10.1016/j.ultras.2015.05.019

[58] Michaels TE, Michaels JE, Ruzzene M. Frequency-wavenumber domain analysis of guided wavefields. Ultrasonics. 2011;**51**:452-466. DOI: 10.1016/j.ultras.2010.11.011

[59] Żak A, Ostachowicz W, Krawczuk M. Damage detection strategies based on propagation of guided elastic waves. Smart Materials and Structures. 2011;**305**:35024. DOI: 10.1088/0964-1726/21/3/035024

[60] Rucka M, Wojtczak E, Lachowicz J. Damage imaging in Lamb wave-based inspection of adhesive joints. Applied Sciences. 2018;**8**:522. DOI: 10.3390/app8040522

[61] Ruzzene M. Frequency-wavenumber domain filtering for improved damage visualization. Smart Materials and Structures. 2007;**16**:2116-2129. DOI: 10.1088/0964-1726/16/6/014

[62] Kudela P, Radzieński M, Ostachowicz W. Identification of cracks in thin-walled structures by means of wavenumber filtering. Mechanical Systems and Signal Processing. 2015;**50-51**:456-466. DOI: 10.1016/j.ymssp.2014.05.041

[63] Harley JB, Chen CC. Statistical partial wavefield imaging using Lamb wave signals. Structural Health Monitoring. 2017. DOI: 10.1177/1475921717727160

[64] Kudela P, Radzienski M, Ostachowicz W, Yang ZB. Structural health monitoring system based on a concept of Lamb wave focusing by the piezoelectric array. Mechanical Systems and Signal Processing. 2018;**108**:21-32. DOI: 10.1016/j.ymssp.2018.02.008

[65] Pai PF, Sundaresan MJ. Space-wavenumber and time-frequency analysis for damage inspection of thin-walled structures. Structural Health Monitoring. 2012;**11**:452-471. DOI: 10.1177/1475921711434860

[66] Li FC, Su ZQ, Ye L, Meng G. A correlation filtering-based matching pursuit (CF-MP) for damage identification using Lamb waves. Smart Materials and Structures. 2006;**15**:1585-1594. DOI: 10.1088/0964-1726/15/6/010

[67] Hu N, Cai YD, Zhu GJ, Tsuji C, Liu YL, Cao YP. Characterization of damage size in metallic plates using Lamb waves. Structural Health Monitoring. 2012;**11**:125-137. DOI: 10.1177/1475921711414230

[68] Perelli A, De Marchi L, Flamigni L, Marzani A, Masetti G. Best basis compressive sensing of guided waves in structural health monitoring. Digital Signal Processing. 2015;**42**:35-42. DOI: 10.1016/j.dsp.2015.04.001

[69] Tofeldt O, Ryden N. Lamb wave phase velocity imaging of concrete plates with 2D arrays. Journal of Nondestructive Evaluation. 2018;**37**(4):13. DOI: 10.1007/s10921-017-0457-x

[70] Staszewski WJ. Advanced data pre-processing for damage identification based on pattern recognition. International Journal of Systems Science. 2000;**31**:1381-1396. DOI: 10.1080/00207720050197776

[71] Maria ML, Kolios AJ, Wang L. Structural health monitoring of off shore wind turbines: A review through the statistical pattern recognition paradigm. Renewable and Sustainable Energy Reviews. 2016;**64**:91-105. DOI: 10.1016/j.rser.2016.05.085

[72] Qiu L, Yuan SF, Chang FK, Bao Q, Mei HF. On-line updating Gaussian mixture model for aircraft wing spar damage evaluation under time-varying boundary condition. Smart Materials and Structures. 2014;**23**. DOI: 10.1088/0964-1726/23/12/125001

[73] Wang Q, Ma SX, Yue D. Identification of damage in composite structures using Gaussian mixture model-processed Lamb waves. Smart Materials and Structures. 2018;**27**:45007. DOI: 10.1088/1361-665X/aaaf96

[74] Staszewski WJ. Intelligent signal processing for damage detection in composite materials. Composites Science and Technology. 2002;**62**:941-950. DOI: 10.1016/S0266-3538(02)00008-8

[75] Suykens JAK, Gestel TV, Brabanter JD, Moor BD, Vandewalle J. Least squares support vector machines. International Journal of Circuit Theory and Applications. 2002;**27**:605-615. DOI: 10.1142/9789812776655

[76] Agarwal S, Mitra M. Lamb wave based automatic damage detection using matching pursuit and machine learning. Smart Materials and Structures. 2014;**23**:85012. DOI: 10.1088/0964-1726/23/8/085012

[77] Das S, Chattopadhyay A, Srivastava AN. Classifying induced damage in composite plates using one-class support vector machines. AIAA Journal. 2010;**48**:705-718. DOI: 10.2514/1.37282

[78] Park S, Yun CB, Roh Y, Lee JJ. PZT-based active damage detection techniques for steel bridge components. Smart Materials and Structures. 2006;**15**:957-966. DOI: 10.1088/0964-1726/15/4/009

[79] Park S, Lee JJ, Yun CB, Inman DJ. A built-in active sensing system-based structural health monitoring technique using statistical pattern recognition. Journal of Mechanical Science and Technology. 2007;**21**:896-902. DOI: 10.1007/BF03027065

[80] Sun FQ, Wang N, He JJ, Guan XF, Yang JS. Lamb wave damage quantification using GA-based LS-SVM. Materials. 2017;**10**:648. DOI: 10.3390/ma10060648

[81] Yang JS, He JJ, Guan XF, Wang DJ, Chen HP, Zhang WF, Liu YM. A probabilistic crack size quantification method using in-situ Lamb wave test and Bayesian updating. Mechanical Systems and Signal Processing. 2016;**78**:118-133. DOI: 10.1016/j.ymssp.2015.06.017

[82] Chiachio J, Bochud N, Chiachio M, Cantero S, Rus G. A multilevel Bayesian method for ultrasound-based damage identification in composite laminates. Mechanical Systems and Signal Processing. 2017;**88**:462-477. DOI: 10.1016/j.ymssp.2016.09.035

[83] He S, Ng CT. Guided wave-based identification of multiple cracks in beams using a Bayesian approach. Mechanical Systems and Signal Processing. 2017;**84**:324-345. DOI: 10.1016/j.ymssp.2016.07.013

[84] Peng TS, Saxena A, Goebel K, Xiang YB, Sankararaman S, Liu YM. A novel Bayesian imaging method for probabilistic delamination detection of composite materials. Smart Materials and Structures. 2013;**22**:125019. DOI: 10.1088/0964-1726/22/12/125019

[85] Neerukatti RK, Hensberry K, Kovvali N, Chattopadhyay A. A novel probabilistic approach for damage localization and prognosis including temperature compensation. Journal of Intelligent Material Systems and Structures. 2016;**27**:592-607. DOI: 10.1177/1045389X15575084

[86] Sohn H, Park HW, Law KH, Farrar CR. Combination of a time reversal process and a consecutive outlier analysis for baseline-free damage diagnosis. Journal of Intelligent Material Systems and Structures. 2006;**18**:335-346. DOI: 10.1177/1045389X06066291

[87] Lu Y, Ye L, Su ZQ, Zhou LM, Cheng L. Artificial neural network (ANN)-based crack identification in aluminum plates with Lamb wave signals. Journal of Intelligent Material Systems and Structures. 2008;**20**:39-49. DOI: 10.1177/1045389X07088782

[88] Legendre S, Massicotte D, Goyette J, Bose TK. Neural classification of Lamb wave ultrasonic weld testing signals using wavelet coefficients. IEEE Transactions on Instrumentation and Measurement. 2001;**50**:672-678. DOI: 10.1109/19.930439

[89] Su ZQ, Ye L. Lamb wave-based quantitative identification of delamination in CF/EP composite structures using artificial neural algorithm. Composite Structures. 2004;**66**: 627-637. DOI: 10.1016/j.compustruct.2004.05.011

[90] Su ZQ, Ye L. Lamb wave propagation-based damage identification for quasi-isotropic CF/EP composite laminates using artificial neural algorithm: Part II - implementation and validation. Journal of Intelligent Material Systems and Structures. 2005;**16**:113-125. DOI: 10.1177/1045389X05047600

[91] De Fenza A, Sorrentino A, Vitiello P. Application of artificial neural networks and probability ellipse methods for damage detection using Lamb waves. Composite Structures. 2015;**133**:390-403. DOI: 10.1016/j.compstruct.2015.07.089

[92] Park SH, Yun CB, Roh Y. PZT-induced Lamb waves and pattern recognitions for on-line health monitoring of jointed steel plates. In: Proceedings of the Smart Structures and Materials 2005 Conference; 07–10 March 2005; San Diego. Bellingham: SPIE Press; 2005. pp. 364-375

[93] Yuan SF, Wang L, Peng G. Neural network method based on a new damage signature for structural health monitoring. Thin-Walled Structures. 2005;**43**:553-563. DOI: 10.1016/j.tws.2004.10.003

[94] Liew CK, Veidt M. Guided waves damage identification in beams with test pattern dependent series neural network systems. WSEAS Transactions on Signal Processing. 2008;**4**:86-96

[95] Anaya M, Tibaduiza DA, Pozo F. Detection and classification of structural changes using artificial immune systems and fuzzy clustering. International Journal of Bio-Inspired Computation. 2017;**9**:35-52. DOI: 10.1504/IJBIC.2017.10002804

[96] Yuan L, Yuan Y, Hernández Á, Shi L. Feature extraction for track section status classification based on UGW signals. Sensors. 2018;**18**:1225. DOI: 10.3390/s18041225

IntechOpen